Consolidation and compression of deformable impregnated fibrous reinforcements: Experimental study and modeling of flow-induced deformations

A. Hautefeuille, Sebastien Comas-Cardona, C. Binetruy

Version of Record: https://www.sciencedirect.com/science/article/pii/S1359835X20300063
Manuscript_10a87dfaf2e190337c7bacbad974071f

Consolidation and compression of deformable impregnated fibrous reinforcements: Experimental study and modeling of flow-induced deformations

A. Hautefeuille[a,*], S. Comas-Cardona[a], C. Binetruy[a]

[a]*GeM - Research Institute of Civil Engineering and Mechanics, UMR 6183, CNRS - École Centrale de Nantes, 1 rue de la Noé, 44321 Nantes, France*

Abstract

Continuous fiber-reinforced thermoplastic composites can be produced by compression or consolidation processes at a temperature above the thermoplastic melting temperature. High production rates or high fluidity thermoplastic (TP-HF) viscosities can lead to large in-plane displacements of the fibrous network during the process. The same mechanisms appear when viscous toughened thermosets resins are used. One can assume that the in-plane displacements occur when the liquid thermoplastic flow sets the deformable fibrous reinforcement in motion. The composite material being manufactured is therefore subjected to a hydro-mechanical coupling between a liquid flow and a deformable continuous fibre reinforcement. Within this context, the in-plane flow-induced deformations during transverse consolidation are investigated in this study. An experimental setup is used in order to localize and quantify fibre tow displacements and large strains as a transient full-field measurement. Then, in order to identify the driving forces occurring during consolidation, these induced deformations are taken into account in the modeling. The fibrous reinforcement properties are redefined locally based on the measured full-field strains. The comparison of experimental and modeling results shows that the local in-plane drag force peaks mainly drive the onset of the fibrous architecture deformation.

Keywords: , B. Optical techniques, D. Process monitoring, C. Process modeling, E. Consolidation

1. Introduction

Structural composites are often processed from pre-impregnated semi-products (prepregs) which consist of a blend of continuous or discontinuous fiber reinforcements, an organic matrix and residual air. Then the composite process aims at evacuating most of the residual air during a compression [1, 2, 3, 4, 5] or a consolidation step [6, 7, 8, 9]. The consolidation or compression, driven and controlled by a transverse out-of-plane unidirectional compaction, generates a flow of the matrix (liquid at the process temperature) within the fibrous reinforcement [10]. The consolidation phase is completed when the saturated fibrous medium reaches the targeted fibre volume fraction of the final composite part.

The saturated fibrous reinforcement can be subjected to two different regimes of in-plane flows during the consolidation [11, 12, 13]. When the fluid drag force is lower than the cohesion forces of the fibrous structure, the liquid flows through an in-plane static fibrous medium. This regime of flow is named a percolation or filtration flow. It guarantees the manufacturing of a flawless structural composite part since its fibrous orientation is maintained. Another regime occurs when the fluid drag force is greater than the cohesion forces of the fibrous reinforcement. The fluid flow has the ability to drag the fibre tows of the reinforcement: flow-induced displacements develop (Fig. 1). They modify the fibrous architecture and the orientations of the tows of the final part. Sometime both regimes occur, as illustrated in Fig. 1, where an in-plane flow is generated by transverse (z-direction) compression. The figure shows that a filtration flow occurs in the y-direction while the squeeze flow drags the fibers in the x-direction. Therefore, the transient hydro-mechanical coupling involved during the consolidation of saturated fiber reinforcements must be studied and controlled because it plays a crucial role in the quality of the produced final composite part.

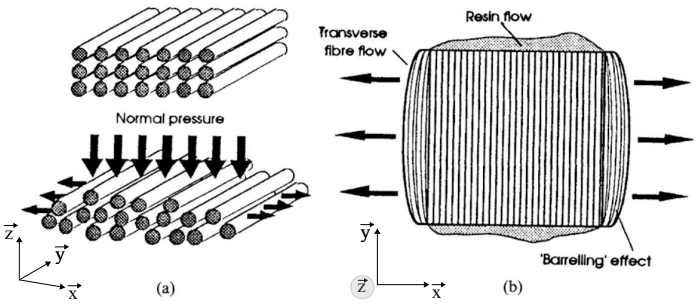

Figure 1: Flow-induced displacement of the fibers during transverse consolidation driven by normal pressure, a) 3D view, b) top view. [12]

*Corresponding author
Email address: alexandre.hautefeuille@ec-nantes.fr (A. Hautefeuille)

2. Previous work and objectives

Fiber-reinforced composite material processes can be divided in processes in which (i) the dry fibers are progressively impregnated or (ii) pre-impregnated fiber reinforcements are used.

The first category includes the Liquid Composite Molding (LCM) processes and among them the Resin Transfer Molding (RTM). During RTM the resin injection can be initiated in the plane or perpendicularly to the plane of the dry fibrous reinforcements maintained in a constant cavity thickness. Some experimental evidences have highlighted the capability of the fluid flow to induce a fibrous reinforcement displacement (washout) in both configurations of injections. An early observation of the washout phenomenon was made by Han et al. [14], who highlighted the capacity of the fluid to induce a segregation in the thickness between a fiber-free region and the fibre-bed during a liquid injection orthogonal to the plane. The deflection of the fiber reinforcement and the flow front were measured thanks to a camera through a transparent mold as the injection was performed. In the case of sandwich processing, the resin-flow-induced displacements of both the sandwich foam core and the fiber reinforced skins have been measured by Al-Hamdan et al. [15] (dynamically thanks to LVDTs) and by Wirth et al. [16] (thanks to microscopy after demolding). For in-plane injections, Endruweit et al. [17] observed visually the flow-induced in-plane displacement of the fibrous reinforcement during the injection. They found that the higher the fiber volume fraction, the lower the in-plane deformation. They also modeled the competition between frictional and viscous forces experienced by a fibrous reinforcement. Seong et al. further [18] developped the experimental bench in order to measure the in-plane transient displacement of the fiber reinforcement during while the impregnation at constant flow rate was occurring. The found that changing the orientation of the fibers from 0° to 45° to 90° increases the flow-induced in-plane displacements.

Some studies have covered other LCM processes such as transverse (out-of-plane) 1D impregnation by compression. Sommer and Mortensen experimented the forced unidirectional infiltration of deformable porous media (sponge) by a liquid a flow (ethylene glycol) [19]. They measured the impregnation rate and the 1D out-of-plane deformation of the porous media with a video camera. They noted that the permeability cannot be taken as constant if the deformation of the porous medium appears significant. They used the Kozeny-Carman relationship for the permeability as the fibre volume fraction is locally slightly modified as the foam deforms. A recent study [20] numerically investigated the large deformations of a soft porous material and used the same relation as a local variation of the permeability. Michaud et al. also experimentally observed the 1D compaction and decompaction occuring during the transverse impregnation of liquid within a fiber reinforcement with a video camera [21]

For the second category of processes such as consolidation by means of compression of pre-impregnated fibrous reinforcements, the literature is more sparse concerning the in-plane deformation measurements. A range of experiments has been presented by Nixon-Pearson in order to study the consolidation behaviour of uncured pre-impregnated fibrous reinforcements [9]. This study exhibits, from post-process micrographs, both bleeding and squeezing flow mechanisms during the compaction phase of the process. At a larger scale, the transverse shear flow of a viscous unidirectional laminated prepreg has been depicted by Sorba et al. using thin copper wires as tracers in the inter-ply of the fibrous architecture [5]. Also a through-thickness analysis has been employed by Hubert to experimentally quantify the in-plane deformation of a unidirectional thermoset prepregs [22]. The latter study proved that percolation flow and shear flow coexist and depend on fluid viscosity, fibre orientation and fibre bed constriction. Barnes and Cogswell [13] and later Murtagh et al. [23] performed squeeze-flow measurements on thermoplastic unidirectional prepregs. They dynamically measured the lateral in-plane displacements at the sample boundaries as the prepreg was compacted. Hautefeuille et al. developed a real-time monitoring and full-field measurement of the in-plane fibre tows movements during transverse consolidation [24]. They also retrieved the mechanical signature of the washout phenomenon (reduced compression response) and linked this signature to fibre-tows displacements.

Within this context of in-plane flow-induced deformations of fiber reinforcements during consolidation, the two main objectives are to:

- Provide a generic method to measure the deformation fields of any reinforcement as a real time monitoring during consolidation (section 3);
- Identify and localize the driving force inducing the displacements (washout) (section 4)

3. Real time monitoring of flow-induced in-plane deformations

3.1. Materials

A quasi uni-directional weft glass fabric UDT 400P (400 g/m^2 weft + 20 g/m^2 warp) from CHOMARAT is used as fibrous material. It differs from the twill-weaved one studied in [24] to underline that the proposed method can be applied to any fabric. Rectangular samples investigated in this study are unidirectional 6-ply stack of planar dimensions 40×22 cm. The components of the in-plane hydraulic permeability tensor of such sample are measured by a method presented in [25] that gives the two in-plane principal permeabilities for orthotropic fibrous reinforcements. The in-plane components (in m^2) of the permeability tensor are fitted to the measured data:

$$\begin{aligned} K_1(V_f) &= 1.2 \times 10^{-11} V_f^{-3.8} - 3.1 \times 10^{-11} \\ K_2(V_f) &= 1.8 \times 10^{-12} V_f^{-4.0} - 5.2 \times 10^{-12} \end{aligned} \quad (1)$$

where V_f is the fibre volume fraction, K_1 the fibre-tow direction (weft) permeability and K_2 the orthogonal one (warp). The permeability tensor is measured for $0.30 \leqslant V_f \leqslant 0.60$.

The fibrous reinforcements samples are saturated with a calibrated silicone oil (from Roth company) corresponding to a fluid fraction $\phi_l^s = 65 \pm 2\%$ and a fibre volume fraction $V_f^s = 35 \pm 2\%$. Each oil viscosity has been measured with a Brookfield DV1 viscometer at room temperature (21°C) and reported in Table 1.

3.2. Experimental procedure

A large-scale semi-transparent test bench has been developed in a previous study [24] in order to continuously track the in-plane motion of the fibre-tows occurring during a saturated transverse compression. The set-up is used with a $L_x = 36$ cm and $L_y = 18$ cm rectangular compression platen. The following Fig. 2 illustrates the elements and systems of the experimental setup.

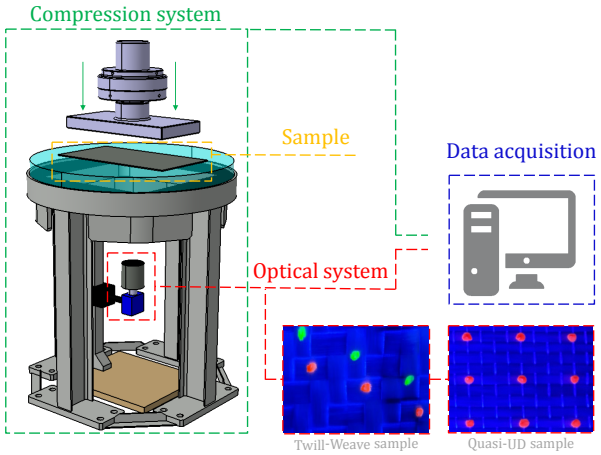

Figure 2: Experimental set-up

An SVS-ECO834 color camera (12 Mpx) with a 16 mm Muytron low-distortion objective is used as optical system. The precision of the measured kinematic fields is related to the resolution of the raw images. The optical uncertainty of the displacement measurement has been quantified to $\Delta = 0.12$ mm for the presented experiments. Two experimental conditions are discussed here, where process parameters are reported in Table 1. The first compression experiment (Exp. 1) is carried out with a low viscosity fluid while in the second one (Exp. 2) a higher fluid stress is generated on the fibrous reinforcement due to a higher viscosity.

Table 1: Experimental parameters

Parameter	Exp. 1	Exp. 2
Fibrous reinforcement	UDT400P	UDT400P
Lay-up	$[90]_6$	$[90]_6$
Compression speed ($\lvert\dot{h}\rvert$)	1.5 mm/min	1.5 mm/min
Fluid viscosity (μ)	0.09 Pa.s	4.58 Pa.s
Fibre fraction at saturation (V_f^s)	35%	35%
Temperature (T)	21°C	21°C

3.3. Displacement field computation

An in-house algorithm has been developed [24] in order to compute the in-plane (x, y) displacement field of the fibre tows during the transverse (z) consolidation imposed by the compression platen. The algorithm is based on tracking and registration techniques for the measurement of the displacement of a particle-cloud, represented by the UV-reactive markers added to the fibrous architecture (top of Fig. 3), between two images. The motion tracking pattern and an example of nodal displacement of a unit cell is shown at the bottom of Fig. 3.

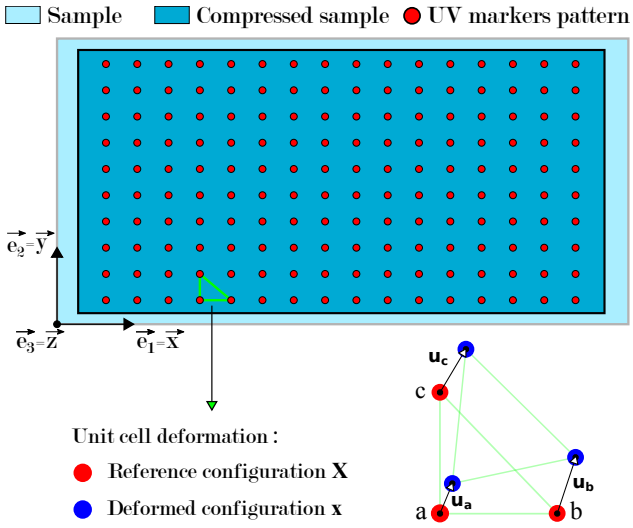

Figure 3: Illustration of in-plane (x, y) motion tracking pattern (top) and example of nodal displacements of a unit cell, from the reference configuration to the deformed one (bottom)

In Fig. 3, for each particle, the position of the node in the deformed configuration (x_n, y_n), can be computed from the reference position of the node (X_n, Y_n) and the nodal displacement (u_n, v_n). This relation explicitly writes in the Cartesian coordinates frame $(\vec{x}, \vec{y})$:

$$\begin{bmatrix} x_n \\ y_n \end{bmatrix} = \begin{bmatrix} X_n \\ Y_n \end{bmatrix} + \begin{bmatrix} u_n \\ v_n \end{bmatrix} \text{ or } \mathbf{x} = \mathbf{X} + \mathbf{u} \tag{2}$$

where $\mathbf{x}$ is the position vector of the node in the deformed configuration at any step of the consolidation, $\mathbf{X}$ the position of the material point in the reference configuration and $\mathbf{u}$ the displacement vector. The complete displacement field is then calculated on raw images at the nodes (UV-markers) and interpolated on the compression surface. Constant strain triangles and first order shape functions are used to compute the strain-field, based on the nodes displacement triangulation, presented in section 3.5. Fig. 4 presents the displacement field and the shape of reconstructed fibre tows of the sample during the consolidation, at different time steps, for both Exp. 1 and Exp. 2. In this figure, the dashed line represents the boundary of the compression platen applying the consolidation stress on the top face of the sample. The corresponding fibre volume fraction, normal force and applied stress are also indicated for each snapshot.

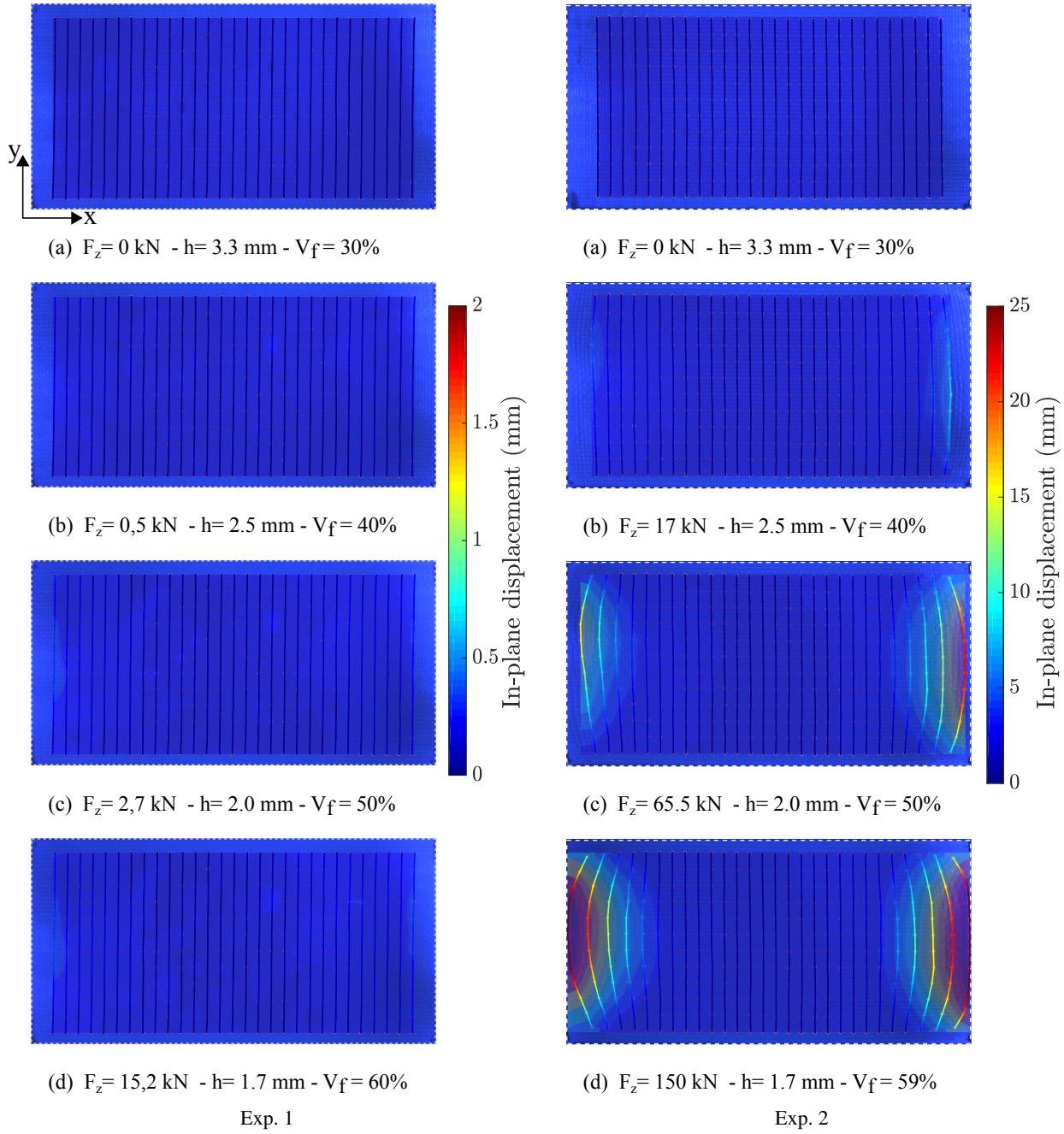

Figure 4: Displacement field computed for Exp. 1 (left) and Exp. 2 (right) at stages V_f = 30, 40, 50 and 60%. of the consolidation

As shown in Fig. 4, two kinds of in-plane flow may occur during the consolidation of the reinforcement. First a percolation flow (i.e flow of the resin through an in-plane static fibre bed) is generated in Exp. 1 (left of Fig. 4). As a matter of fact, the measured in-plane displacement of the fibre tow is negligible at the scale of fibre tows because these latter do not move. However, in Fig. 4 (right), Exp. 2 displays progressive in-plane displacements up to 25 mm at the end of the experiment. As the flow-induced deformations are addressed in this study, the analysis of Exp. 2 will be performed in the following. From those results, one can sense that the fibre tows washout distance is macroscopically symmetrical with respect to the part center and increases with the distance from that point. However, a thin asymmetry of the washout distance is noticed on experimental results, likely due to the geometrical variability of the fibrous reinforcement. Also, while the experimental conditions impose null fluid pressure and gradient outside the compression platens, this boundary represents a limit to the fibres movement. This phenomenon can be observed in the end stages of Exp. 2 in Fig. 4. One can see in (d) of Exp. 2 that the tows accumulate at the edge of the compression platen.

3.4. Solid velocity computation

The velocity field of the fibrous reinforcement is calculated by temporal derivation of the displacement field. The Fig. 5 presents the Euclidean norm of the fibre tows in-plane velocity at several steps of the consolidation process.

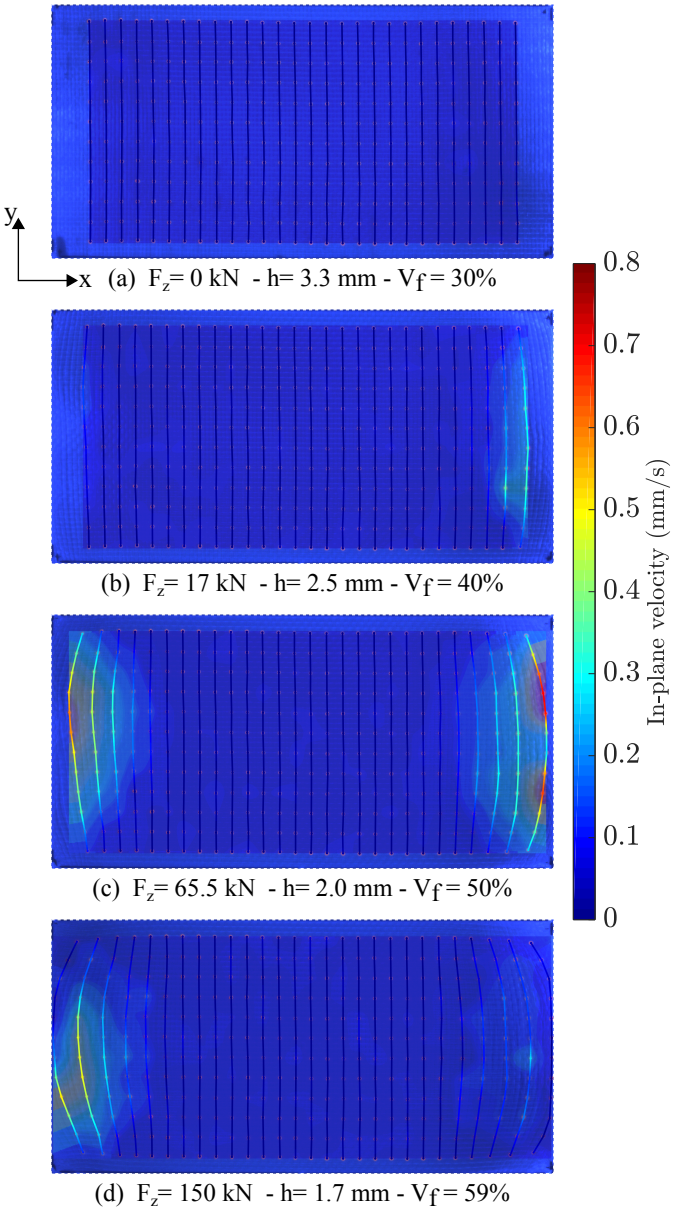

Figure 5: In plane tows velocity for Exp. 2 at stages $V_f = 30, 40, 50$ and 59% of the consolidation

Measurements show that for this test configuration, the solid velocity in-plane magnitude remains below 0.75 mm/s during the consolidation process. An acceleration of the tows occur between steps (b) and (c) of the consolidation, which can be attributed to the setting in motion of the fibrous architecture. At the final stages of the consolidation, the in-plane velocity of the tows decreases. This phenomenon results from the combination of two phenomena. First, once the deformations have become significant within the fibrous architecture, the viscous drag forces are expected to drop. This point is further discussed in section 4.3. Secondly, the friction forces are most likely high in the final stages of the consolidation (friction forces are directly related to the compressive force by friction law).

3.5. Deformation field computation

3.5.1. Green-Lagrange strain tensor

Data reported in section 3.3 showed that the fibrous reinforcement is subjected to large strains. As the displacement field $\mathbf{u}$ includes rigid body motions, one must use the deformation-gradient tensor $\mathbf{F}$ that excludes rigid body translations to extract the deformations. The deformation-gradient tensor $\mathbf{F}$ writes:

$$\mathbf{F} = \nabla \mathbf{u} + \mathbf{I} \tag{3}$$

where $\mathbf{u}$ is the particle-cloud displacement field and $\mathbf{I}$ the second order identity tensor. Then, the Green-Lagrange strain tensor $\mathbf{E}$ is used in this study for its capacity to fully eliminate the remaining rigid body rotations. Based on the deformation-gradient $\mathbf{F}$, the Green-Lagrange strain tensor $\mathbf{E}$ writes:

$$\mathbf{E} = \frac{1}{2}\left(\mathbf{F}^T \cdot \mathbf{F} - \mathbf{I}\right) = \frac{1}{2}\left(\mathbf{C} - \mathbf{I}\right) \tag{4}$$

where $\mathbf{C}$ is the right Cauchy-Green deformation tensor. For a $\mathbf{u} = (u, v)$ displacement field, the explicit expressions of the components of the 2D Green-Lagrange strain tensor E_{ij} are written in Eqs (5-7). Note that as the strains are large (finite), the components of the Green Strain tensor contain small (first order) strain contributions and quadratic ones.

$$E_{xx} = \frac{\partial u}{\partial X} + \frac{1}{2}\left[\left(\frac{\partial u}{\partial X}\right)^2 + \left(\frac{\partial v}{\partial X}\right)^2\right] \tag{5}$$

$$E_{yy} = \frac{\partial v}{\partial Y} + \frac{1}{2}\left[\left(\frac{\partial u}{\partial Y}\right)^2 + \left(\frac{\partial v}{\partial Y}\right)^2\right] \tag{6}$$

$$E_{xy} = \frac{1}{2}\left(\frac{\partial u}{\partial Y} + \frac{\partial v}{\partial X}\right) + \frac{1}{2}\left[\frac{\partial u}{\partial X}\frac{\partial u}{\partial Y} + \frac{\partial v}{\partial X}\frac{\partial v}{\partial Y}\right] \tag{7}$$

In the experimental configuration of Exp. 2, the E_{xx} component is orthogonal to the fibre tows while the E_{yy} component is co-linear to them. The E_{xy} component represents the shear of the fibrous architecture. The E_{xx} component is predominant in this experimental configuration due to the axial inextensibility of fibre tows. Fig. 6 presents the E_{xx} component field of the sample during Exp. 2, at several stages of the consolidation. In addition to the in-plane (x, y) full-field measurements, the total compression force F_z and the thickness h are reported at each stage of consolidation.

From those results, one can conclude that the in-plane fibre tows transverse deformation E_{xx} follows a different behaviour depending on its position along x. The induced deformation of the fabric propagates towards the center of the sample during consolidation. In addition, this deformation peaks at the edge of the part due to the stopping of the fibre tows at the edge of the compression plate.

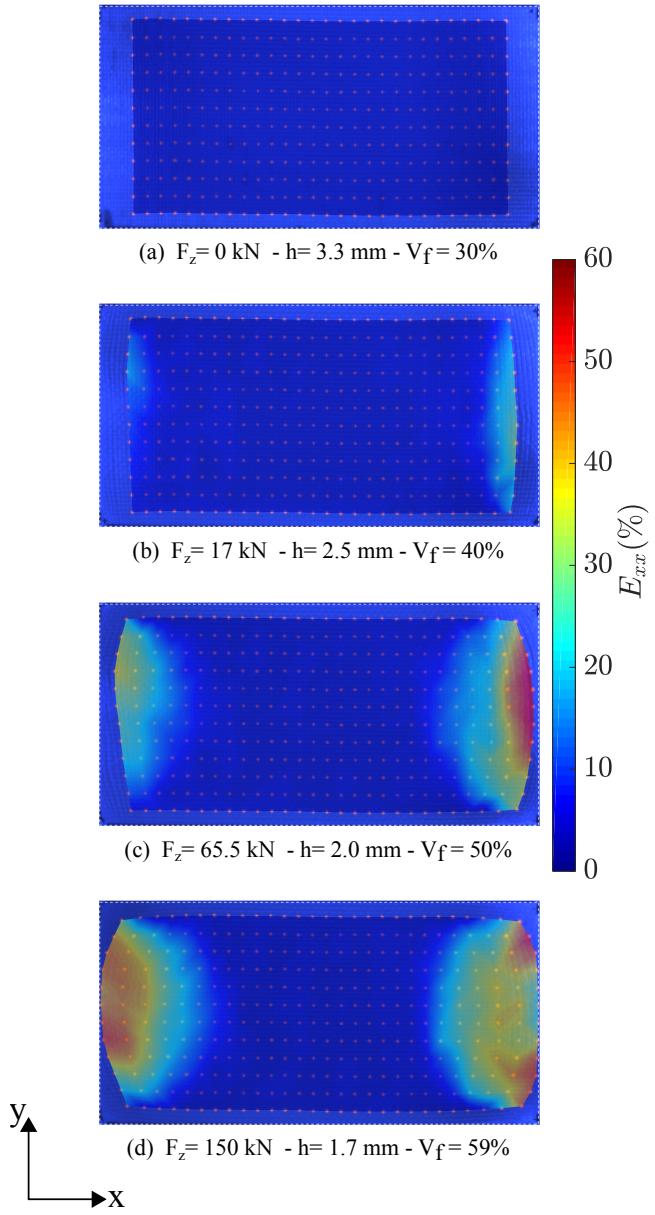

Figure 6: E_{xx} field computed for Exp. 2 at $V_f = 30, 40, 50$ and 59%

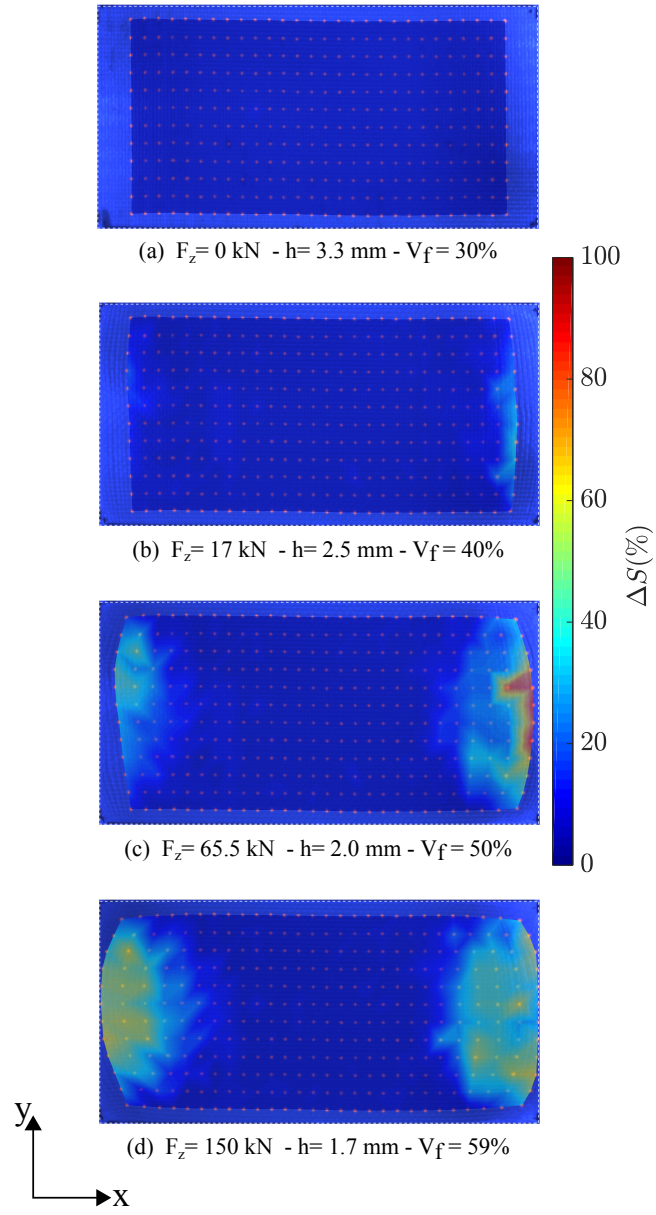

Figure 7: ΔS field computed for Exp. 2 at $V_f = 30, 40, 50$ and 59%

3.5.2. Local area variation

The measurement of the local area variation ΔS on the sample area can be expressed as the ratio between the area of a deformed material mesh element to its area in the initial configuration defined by the UV markers (Fig. 3). The Jacobian determinant $\mathbf{J}$ expresses this ratio and reads as:

$$\Delta S = \mathbf{J}(\mathbf{x}, i) = det(\mathbf{F}) \tag{8}$$

where $\mathbf{\Delta S}$ is the normalized local area variation, $\mathbf{J}$ is the Jacobian determinant and $(\mathbf{x}, i)$ the position of the material point in the 2D surface at the i^{th} step of the consolidation. Fig. 7 presents the local area variation $\mathbf{\Delta S}$ during consolidation at $V_f = 30, 50$ and 59%, in Exp. 2.

One can observe a maximum of 40% of surface increase for most of off-centred regions. In the case of deformable and compliant porous media such as continuous fibre reinforcements, the solid constituents (fibres) and the fibre tows are unstrechable along their length. Then all the deformations consist in the rearrangement of the tows and the resulting macroscopic porous network. The experimental methods described in this section paved the way to localize the in-plane displacement, deformation and solid velocity magnitude as a continuous field measurement during the consolidation of saturated fibrous reinforcement. This local tows reorganization modifies the properties of the fibrous material as described in the next section.

4. Modeling

The experimental results presented above revealed that the material undergoes local non-homogeneous in-plane deformations during consolidation. Identification of the in-plane washout driving force requires to take into account these local changes. Starting from the local modification of the geometric properties of the material (fibre content and then permeability), the pressure field in the deformed sample is computed for each step of the consolidation. From this pressure field the pressure gradient field is extracted, thus allowing the identification of the viscous drag force field.

4.1. Local modification of the material properties

The measured deformations are projected onto an interpolation grid, used to locally redefine the material properties. Fig. 8 shows the projection method of the deformations measured on the interpolation grid of 100×100 elements.

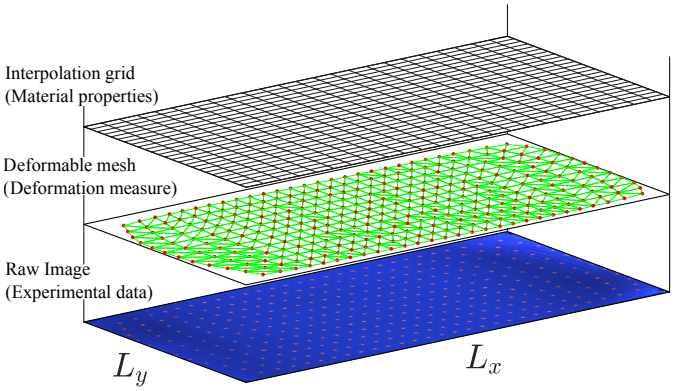

Figure 8: Material properties grid

As the UV marker pattern does not cover the entire consolidation surface, a "nearest value" extrapolation is performed on the non-measured zones in order to define material properties on the entire consolidation surface. The extrapolation surface decreases from 25% in the early stages to 15% of the compression surface at the end stages of the experiment, the deformable mesh covering more and more surface area all along the experiment.

4.1.1. Fibre volume fraction

As during consolidation, the imposed thickness decrease is controlled by the press, the average fibre volume fraction in the fibrous reinforcement evolves as h decreases according to:

$$V_f = \frac{NA_w}{\rho h} \tag{9}$$

where N is the number of plies, A_w the areal weight of a fabric ply, ρ the density of the solid phase constituent (glass fibre here) and h the thickness. This relation leads to a constant spatial fibre volume fraction in the whole specimen during the consolidation. However, the in-plane flow-induced deformations modify the local areal weight and then the local fibre volume fraction according to the position $\mathbf{x}$ of the material point. This modification paves the way to the definition of a fibre volume fraction field $V_f(\mathbf{x}, i)$ for each i step of the consolidation:

$$V_f(\mathbf{x}, i) = \frac{A_w(\mathbf{x}, i)}{A_w^0}.V_f(i) \quad \text{with} \quad A_w(\mathbf{x}, i) = \Delta S(i) \times A_w^0 \tag{10}$$

Or

$$V_f(\mathbf{x}, i) = \mathbf{J}(\mathbf{x}, i).V_f(i) \tag{11}$$

where A_w^0 is the original fibrous reinforcement areal weight, $\Delta S(i)$ is the surface change field at the i step of the consolidation which respectively transforms the original areal weight and global fibre volume fraction into localized one $A_w(\mathbf{x}, i)$ and $V_f(\mathbf{x}, i)$. The Jacobian determinant $\mathbf{J}$ is then directly related to the fibre volume fraction. Fig. 9 illustrates the fibre volume fraction field $V_f(\mathbf{x}, i)$ evolution during the consolidation, at average $V_f = 30,\ 40,\ 50$ and 59%.

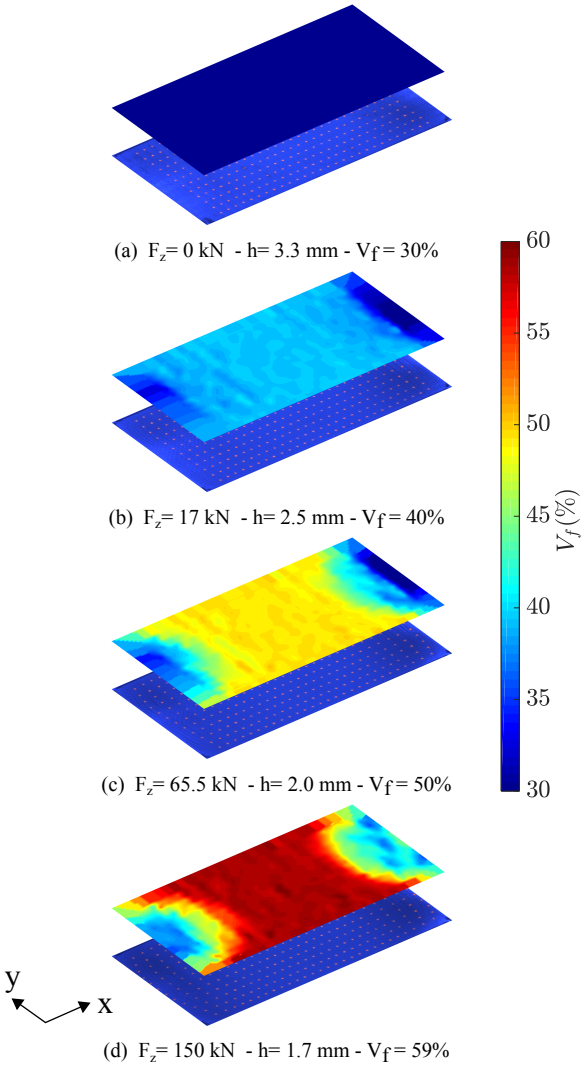

Figure 9: $V_f(\mathbf{x}, i)$ field for Exp. 2 at $V_f = 30,\ 40,\ 50$ and 59%

The results show that for a given thickness, the local fibre volume fraction in the sample can locally vary by 30% for Exp. 2. As a consequence, these large variations induce local changes in the porosity and in the permeability of the sample.

4.1.2. *Permeability in-plane tensor*

If the fibrous reinforcement does not experience any in-plane deformations during the transverse consolidation, the in-plane permeability components can be updated according to:

$$\begin{aligned} K_x &= K_2(V_f) \\ K_y &= K_1(V_f) \end{aligned} \tag{12}$$

where K_1 and K_2 are the reference components of the permeability tensor presented in Eq. (1). If in-plane deformations of occur during the transverse consolidation, the in-plane permeability components are then computed from:

$$\begin{aligned} K_x &= K_2(V_f(\mathbf{x})) \\ K_y &= K_1(V_f(\mathbf{x})) \end{aligned} \tag{13}$$

where $K_1(\mathbf{x})$ and $K_2(\mathbf{x})$ are the permeability fields calculated from the local ($\mathbf{x} = (x, y)$) fibre volume fraction determined in Eq. (10).

This first analysis assumes that in the presence of local in-plane deformations, components of the permeability tensor only depend on the fibre volume fraction. Fig. 10 illustrates results obtained from the raw image to the permeability tensor field for Exp. 2.

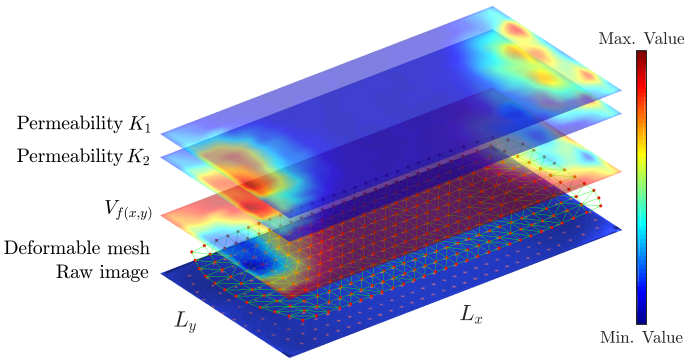

Figure 10: Permeability field identification in the deformed state of the fibrous reinforcement in Exp. 2 (here, $V_f = 59\%$)

This illustration shows that the permeability components are locally increased in regions where the local fibre volume fraction is increased by flow-induced deformations. This effect has repercussions on the whole structure averaged permeability. Fig. 11 illustrates the in-plane permeability components for the undeformed state (Eq. (1)) and the surface averaged one for deformed state of the material for Exp. 2.

At the scale of the whole structure, one can sense that the spatially averaged permeabilities of the deformed fabric are greater than the non-deformed ones.

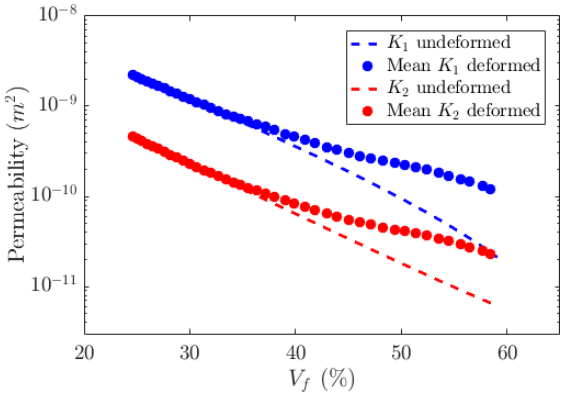

Figure 11: Comparison between the reference permeability (Eq. (1) in undeformed state) and the average of K_1 and K_2 during Exp. 2 (deformed state)

4.2. *Pressure field computation*

For continuous transverse compression of a saturated porous media, the fluid pressure is governed by the continuity equation combined with Darcy's law [10]. Assuming a planar flow, and that the permeability tensor does not rotate (i.e neglecting the off-diagonal K_{xy} terms of the permeability tensor) it writes:

$$\frac{\partial}{\partial x}(K_x \frac{\partial P}{\partial x}) + \frac{\partial}{\partial y}(K_y \frac{\partial P}{\partial y}) = -\mu \frac{\dot{h}}{h} \tag{14}$$

where K_x and K_y are the permeability tensor components in the x and y flow directions, P the fluid pressure, μ the fluid viscosity, $\dot{h}$ the compaction velocity, and h the thickness. In this study, $\frac{\partial K_{x,y}}{\partial x,y}\frac{\partial^2 P}{\partial x^2,y^2} / K_{x,y}\frac{\partial^2 P}{\partial x^2,y^2} \approx 10^{-3}$. Therefore, the consolidation equation simplifies in:

$$K_x \frac{\partial^2 P}{\partial x^2} + K_y \frac{\partial^2 P}{\partial y^2} = -\mu \frac{\dot{h}}{h} \tag{15}$$

The solution of Eq. (15) is calculated by the finite difference method with the use of Successive Over-Relaxation (SOR) iterative method. The pressure field calculated for Exp. 2 from Eq. (13) and Eq. (15) is shown in Fig. 12. The transparent field displayed on the figures is the solution calculated without taking into account the in-plane washout phenomenon (K_x and K_y are spatially constant in Eq. (15) and Eq. (12)).

From these results it can be seen that the fluid pressure profile and intensity are modified as soon as the washout phenomenon is taken into account. The maximum pressure remains centered due to the macroscopic symmetry of the deformation. Also, there is a pressure drop in the deformed areas due to the increased permeability. The integration of the fluid pressure field on the compression surface S_{comp} gives the fluid force F_{fluid}:

$$F_{fluid} = \int_{S_{comp}} P \, \mathrm{d}S_{comp} \tag{16}$$

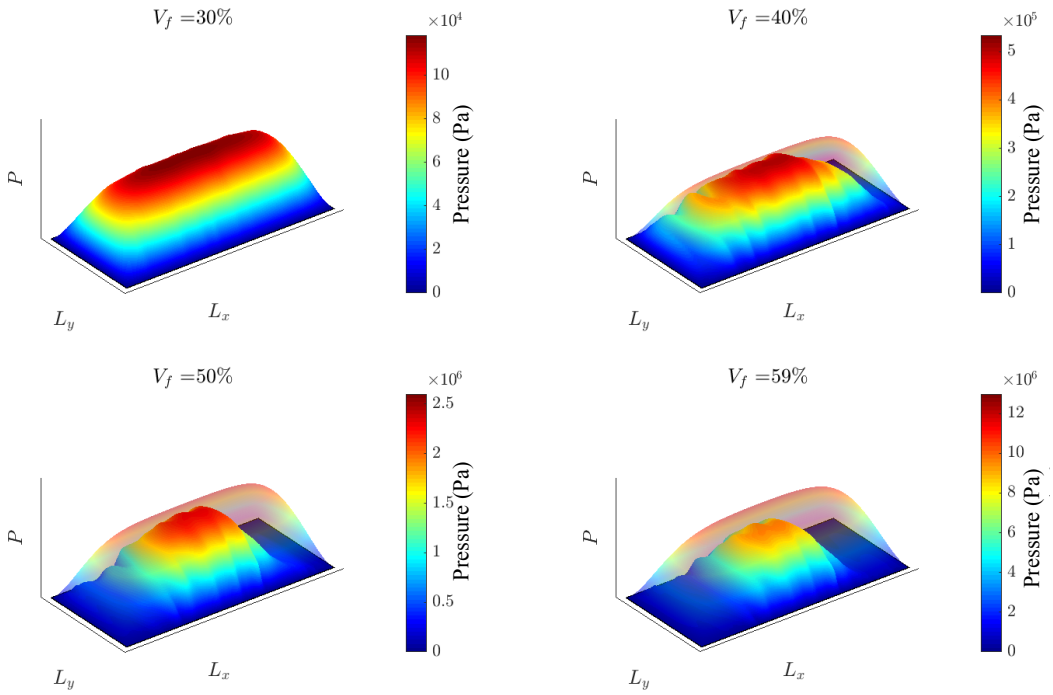

Figure 12: Fluid pressure field for Exp. 2 computed with Eqs.(13 & 15), semi-transparent field refers to the non-deformed case computed with Eqs.(12 & 15)

In Fig. 13, the experimental fluid force obtained for Exp. 2 is compared to Eq. (15) solved with Eq. (12) and then with Eq. (13). The experimental fluid force is obtained by subtracting the lubricated fibrous reinforcement compression response to the total force applied on the sample. The latter compression response being evaluated at the same compression speed. One could use more refined theoretical fibrous response such as the one described in [26].

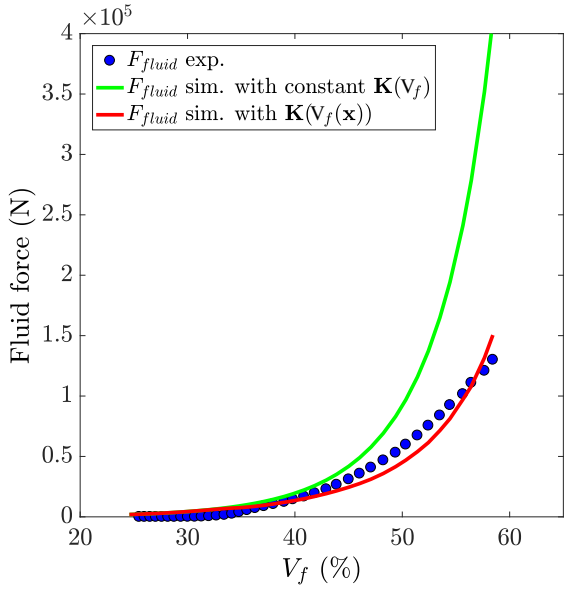

Figure 13: Comparison of the experimental fluid forces for Exp. 2 with the numerical fluid force computed from Eqs.(12 & 15) (constant permeability field) and Eqs.(13 & 15) (variable permeability field)

The average error of each model has been computed for Exp. 2 along the saturated consolidation step ($0.40 \leqslant V_f \leqslant 0.60$). For Exp. 2, the consideration of deformation in the permeability fields reduces the averaged error from 83% to 16%. At first order, taking into account in-plane deformations to calculate the local fibre volume fraction $V_f(\mathbf{x})$ and then the local permeability tensor $\mathbf{K}(\mathbf{x})$ allows a good prediction of the fluid pressure and the force response when flow-induced deformations occur.

4.3. Viscous drag force identification

The flow of a newtonian fluid within a porous medium generates a drag force experienced by the fibrous structure. In [27], Tucker defined the total fluid-solid interaction force $\mathbf{f_T}$ as the result of 3 contributions: the viscous drag force $\mathbf{f_d}$ exerced by the fluid, the gravity-induced pressure gradient in the fluid $\mathbf{f_{gh}}$ and the average effective fluid pressure (form drag) $\mathbf{f_P}$.

$$\mathbf{f_T} = \mathbf{f_d} + \mathbf{f_{gh}} + \mathbf{f_P} \tag{17}$$

As a constitutive modeling, Slattery derived the force exerted upon the solid by the fluid in porous media known as the viscous drag [28]. Under some realistic assumptions, the viscous drag $\mathbf{f_d}$ is assumed to be a function of the velocity of the fluid relative to the solid as well as material parameters such as:

$$\mathbf{f_d} = R\left[< \boldsymbol{v}_l >^l - < \boldsymbol{v}_s >^s\right] \tag{18}$$

where R is considered as a scalar resistance vector which depends on the fluid viscosity, porosity and on local length scale of the porous medium. $<\boldsymbol{v}_l>^l$ and $<\boldsymbol{v}_s>^s$ refer respectively to the intrinsic phase averaged (l and s) liquid and solid velocities.

$\phi<\boldsymbol{v}_l>^l = <\boldsymbol{v}_l>$ is the Darcy's or superficial velocity of the fluid through the pore space. Assuming a proper symetry between the liquid and the solid phase, one can sense that $(1-\phi)<\boldsymbol{v}_s>^s = <\boldsymbol{v}_s>$ [29]. A further dimensional analysis expresses the viscous drag force (force per unit volume in N/m^3) experienced by an homogeneous porous media as [27]:

$$\mathbf{f_d} = \phi\mu\boldsymbol{K}^{-1}\,[<\boldsymbol{v}_l> - <\boldsymbol{v}_s>] \tag{19}$$

where $\boldsymbol{K}$ is the permeability tensor of the porous material. Suggesting that inter-tow flow is very dominant in the case of a dual-scale flow, Pillai retrieved the same expression for flow through woven reinforcement [30]. Using the Darcy's law [31] ($<\boldsymbol{v}_l> - <\boldsymbol{v}_s> = -\frac{\boldsymbol{K}}{\mu}.\nabla P$), the drag force reads:

$$\mathbf{f_d} = -\phi\vec{\nabla}P \tag{20}$$

where $\phi = 1 - V_f$ refers to the porosity of the fibrous medium, and $\vec{\nabla}P$ is the pressure gradient that can be calculated from the solving of Eq. (15).

The non-homogeneous deformation of the fabric gives rise to the form drag $\mathbf{f_P}$, which is related to the gradient of fibre volume fraction in the fabric

$$\mathbf{f_P} = -P\vec{\nabla}\phi \tag{21}$$

where P is the fluid pressure and $\vec{\nabla}\phi$ is the porosity gradient in the porous medium. This contribution can be neglected if the porosity gradient is null or very small in comparison to the viscous drag force $\mathbf{f_d}$. Neglecting the gravity induced pressure gradient ($\mathbf{f_{gh}} = 0$), the total fluid-solid interaction writes:

$$\mathbf{f_T} = \mathbf{f_d} + \mathbf{f_P} = -\vec{\nabla}(\phi P) \tag{22}$$

For Exp. 2, the surface-averaged value of each contribution of the fluid-solid interaction force are computed throughout the entire consolidation experiment and presented in Fig. 14.

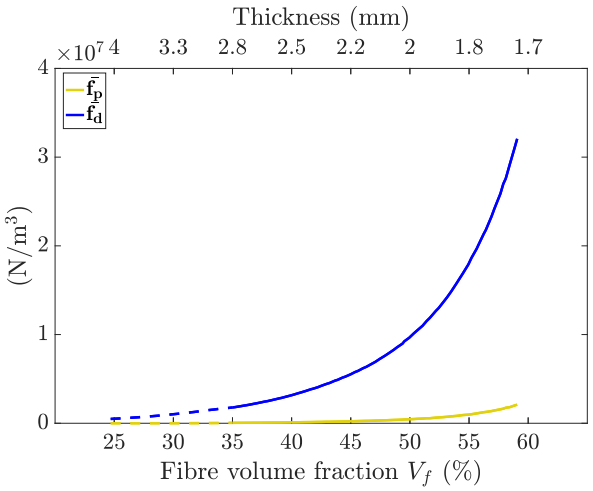

Figure 14: Comparison between the surface-averaged values of the viscous drag force $\mathbf{f_d}$ and the form drag $\mathbf{f_P}$ components of the total fluid/solid interaction force $\mathbf{f_T}$ during the consolidation experiment

Results show that the contribution of the viscous drag force is preponderant in the total fluid-solid interaction force within the fibrous reinforcement. Hence, it is assumed here that the additional form drag $\mathbf{f_P}$ arising from the porosity gradient is marginal compared to the viscous drag force.

Fig. 15 shows the correlation between the mid-width ($y = 0$) x-component of the viscous drag force and the mid-width deformation E_{xx} of the fibrous architecture.

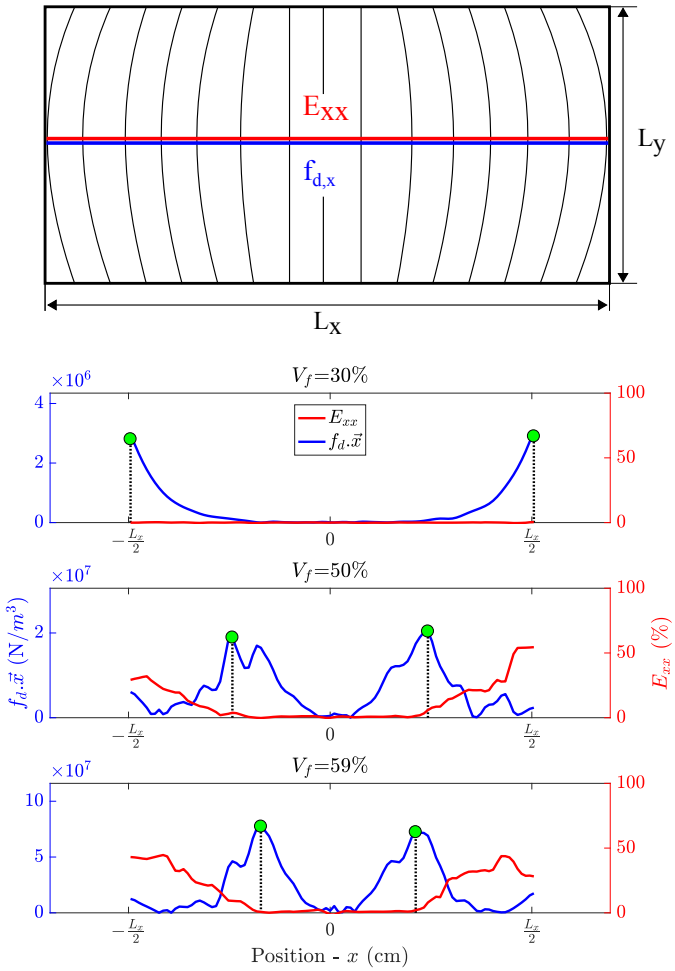

Figure 15: Correlation between the viscous drag force (x direction) and the in-plane (x direction) deformation of the fibrous reinforcement at the mid-width of the part

From the top plot of Fig. 15, at $V_f = 30\%$, the maximum drag force occurs at the edges of the platens. As the consolidation progresses (middle plot, $V_f = 50\%$), the drag force displays 2 peaks (symmetrically to the center of the platen). The location of the 2 peaks corresponds to the location of the onset of the fibrous reinforcement deformation. The bottom plot ($V_f = 59\%$) shows the same behavior but the drag force peaks and deformations are further moved toward the center of the sample. This correlation shows that the in-plane deformation starts where the the viscous drag force reaches a peak. Also, the viscous drag force drops right after the onset of the deformation, which is due to the increase of permeability linked to the deformation. Therefore the viscous drag force

peaks tend to reach the center of the part as the consolidation proceeds. This is due to the re-centering of the pressure gradient maximums as a result of the in-plane deformation of the fibrous architecture.

5. Conclusion

In this study related to impregnated fiber reinforcement sample subjected to consolidation, a method that dynamically measures flow-induced in-plane deformations has first been proposed. Then, the driving forces (drag forces) inducing the fiber tow deformations have been identified and localized. Among the forces applied to the fibrous network, the drag force is greater than the form drag.

Experiments carried out in this study have shown that important changes in fibrous architecture can be caused by the in-plane washout phenomenon. The deformation and area change fields have been computed from the displacement field of the fibre tows using a continuum mechanics based approach. As the consolidation proceeds, deformations propagate in the fibre tow transverse direction, starting at the edge of the sample and propagates towards its center. Once the localization and quantification of these deformations are known, the consolidation is modeled through local modifications of material properties. The areal variation of the material elements locally modify the permeability tensor of the fibrous reinforcement. Also, the solid phase (fiber tows) velocity has been quantified and then neglected in the resolution of the consolidation equation. Neglecting the solid-phase velocity compared with the average local liquid velocity is proved acceptable given the simplicity and agreement with experimental data it provides. Prediction could be refined by taking into account the solid phase velocity field and developing a model to relate the current permeability to the deformed fibrous network. In the longer term, the viscous drag force will be compared to friction forces present in the sample during consolidation. This comparison will pave the way to the control of flow induced deformations during composite manufacturing processes that include a consolidation stage.

Acknowledgements

Part of this study is funded by FUI-AAP20 Regions Projects (France) within the INCREASE project (partners: Solvay, IFTH, Billion SAS, Pernoud, Chomarat Textiles Industries, IPC, INSA Lyon and Centrale Nantes)

Nomenclature

Symbol	Quantity	unit
A_w^0	Native areal weight	kg/m^2
A_w	Areal weight	kg/m^2
$\mathbf{C}$	Right Cauchy-Green tensor	-
$\mathbf{E}$	Green-Lagrange tensor	-
$\mathbf{f_d}$	Viscous drag force	N/m^3
$\mathbf{f_{gh}}$	Gravity-induced pressure gradient	N/m^3
$\mathbf{f_T}$	Fluid-solid interaction force	N/m^3
$\mathbf{f_P}$	Form drag	N/m^3
$\mathbf{F}$	Deformation gradient tensor	-
F_{fluid}	Fluid force exerted on compression platen	N
F_z	Compression force	N
$\mathbf{F}$	Deformation gradient tensor	-
h	Thickness	m
$\dot{h}$	Compression speed	m/s
$\mathbf{I}$	Identity tensor	-
$\mathbf{J}$	Jacobian determinant	-
$\mathbf{K}$	Permeability tensor (2D)	m^2
K_1	Permeability along fibre tows	m^2
K_2	Permeability transverse to fibre tows	m^2
K_x	Permeability along platen length	m^2
K_y	Permeability along platen width	m^2
L_x	Compression platen length	m
L_y	Compression platen width	m
N	Number of plies	-
P	Pressure field	Pa, N/m^2
∇P	Pressure gradient field	Pa/m, N/m^3
S	Area of the compression platens	m^2
ΔS	Local area variation	-
T	Temperature	°C
$\mathbf{u} = (u, v)$	Displacement field	m
$< V_{l,s} >$	phase averaged velocity	m/s
$< V_{l,s} >^{l,s}$	intrinsic phase average	m/s
V_f	Fibre volume fraction	-
V_f^s	Fibre volume fraction at saturation	-
$V_f(\mathbf{x})$	Fibre volume fraction field	-
$\mathbf{x} = (x, y)$	Material position vector	m
$\mathbf{X} = (X, Y)$	Material reference position vector	m
μ	Viscosity	Pa.s
ϕ	Porosity	-
ϕ_l^s	Fluid fraction at saturation	-
ρ	Density	kg/m^3

References

[1] M. Deleglise, C. Binetruy, and P. Krawczak, "Modeling and simulation of liquid compression molding using lims," in 7th International Conference on Flow Processes in Composite Materials (FPCM-7), pp. 347–352, 2004.

[2] P. Bhat, J. Merotte, P. Simacek, and S. G. Advani, "Process analysis of compression resin transfer molding," Composites Part A: Applied science and manufacturing, vol. 40, no. 4, pp. 431–441, 2009.

[3] S. Bickerton and P. Kelly, "Compression resin transfer moulding (crtm) in polymer matrix composites," in Manufacturing techniques for polymer matrix composites (PMCs), pp. 348–380, Elsevier, 2012.

[4] Y. Wang, "Effect of consolidation method on the mechanical properties of nonwoven fabric reinforced composites," Applied Composite Materials, vol. 6, no. 1, pp. 19–34, 1999.

[5] G. Sorba, C. Binetruy, A. Leygue, and S. Comas-Cardona, "Squeeze flow in heterogeneous unidirectional discontinuous viscous prepreg laminates: Experimental measurement and 3d modeling," Composites Part A: Applied Science and Manufacturing, vol. 103, pp. 196–207, 2017.

[6] I. Fernández, F. Blas, and M. Frövel, "Autoclave forming of thermoplastic composite parts," Journal of Materials Processing Technology, vol. 143, pp. 266–269, 2003.

[7] F. C. Campbell Jr, Manufacturing technology for aerospace structural materials. Elsevier, 2011.

[8] T. Centea, L. K. Grunenfelder, and S. R. Nutt, "A review of out-of-autoclave prepregs–material properties, process phenomena, and manufacturing considerations," Composites Part A: Applied Science and Manufacturing, vol. 70, pp. 132–154, 2015.

[9] O. Nixon-Pearson, J.-H. Belnoue, D. Ivanov, K. Potter, and S. Hallett, "An experimental investigation of the consolidation behaviour of uncured prepregs under processing conditions," Journal of Composite Materials, vol. 51, no. 13, pp. 1911–1924, 2017.

[10] T. G. Gutowski, T. Morigaki, and Z. Cai, "The consolidation of laminate composites," Journal of Composite Materials, vol. 21, no. 2, pp. 172–188, 1987.

[11] P. Hubert and A. Poursartip, "A review of flow and compaction modelling relevant to thermoset matrix laminate processing," Journal of Reinforced Plastics and Composites, vol. 17, no. 4, pp. 286–318, 1998.

[12] A. Murtagh and P. Mallon, Characterization of shearing and frictionnal behavior during sheet forming, ch. 5, pp. 163–215. 1997.

[13] J. Barnes and F. Cogswell, "Transverse flow processes in continuous fibre-reinforced thermoplastic composites," Composites, vol. 20, no. 1, pp. 38–42, 1989.

[14] K. Han, L. Trevino, L. J. Lee, and M. Liou, "Fiber mat deformation in liquid composite molding. i: Experimental analysis," Polymer composites, vol. 14, no. 2, pp. 144–150, 1993.

[15] A. Al-Hamdan, C. Rudd, and A. Long, "Dynamic core movements during liquid moulding of sandwich structures," Composites Part A: Applied Science and Manufacturing, vol. 29, no. 3, pp. 273–282, 1998.

[16] S. Wirth, R. Gauvin, and K. Kendall, "Experimental analysis of core crushing and core movementin rtm and srim foam cored composite parts," Journal of reinforced plastics and composites, vol. 17, no. 11, pp. 964–988, 1998.

[17] A. Endruweit, S. Gehrig, and P. Ermanni, "Mechanisms of hydrodynamically induced in-plane deformation of reinforcement textiles in resin injection processes," Journal of composite materials, vol. 37, no. 18, pp. 1675–1692, 2003.

[18] D. G. Seong, S. Kim, M. K. Um, and Y. S. Song, "Flow-induced deformation of unidirectional carbon fiber preform during the mold filling stage in liquid composite molding process," Journal of Composite Materials, vol. 52, no. 9, pp. 1265–1277, 2018.

[19] J. L. Sommer and A. Mortensen, "Forced unidirectional infiltration of deformable porous media," Journal of Fluid Mechanics, vol. 311, pp. 193–217, 1996.

[20] C. W. MacMinn, E. R. Dufresne, and J. S. Wettlaufer, "Large deformations of a soft porous material," Physical Review Applied, vol. 5, no. 4, p. 044020, 2016.

[21] V. Michaud, R. Törnqvist, and J.-A. Månson, "Impregnation of compressible fiber mats with a thermoplastic resin. part ii: Experiments," Journal of composite materials, vol. 35, no. 13, pp. 1174–1200, 2001.

[22] P. Hubert, Aspects of flow and compaction of laminated composite shapes during cure. PhD thesis, University of British Columbia, 1996.

[23] A. Murtagh, A. Mulholland, M. Monaghan, and P. Mallon, "Aspects in sheet-forming characterisation of advanced composites," in Key Engineering Materials, vol. 72, pp. 263–278, Trans Tech Publ, 1992.

[24] A. Hautefeuille, S. Comas-Cardona, and C. Binetruy, "Mechanical signature and full-field measurement of flow-induced large in-plane deformation of fibrous reinforcements in composite processing," Composites Part A: Applied Science and Manufacturing, vol. 118, pp. 213–222, 2019.

[25] B. Martin, S. Comas-Cardona, C. Binetruy, N. Billon, J.-L. Bouvard, and P. Lucas, "Influence of fabrics design parameters on the morphology and 3d permeability tensor of quasi-unidirectional non-crimp fabrics," Composites Part A: Applied Science and Manufacturing, vol. 90, pp. 470–479, 2016.

[26] K. Pillai, C. L. Tucker, and F. Phelan, "Numerical simulation of injection/compression liquid composite molding. part 2: preform compression," Composites Part A: applied science and manufacturing, vol. 32, no. 2, pp. 207–220, 2001.

[27] C. Tucker, R. Dessenberger, et al., "Governing equations for flow and heat transfer in stationary fiber beds," Composite Materials Series, pp. 237–257, 1994.

[28] J. C. Slattery, "Single-phase flow through porous media," AIChE Journal, vol. 15, no. 6, pp. 866–872, 1969.

[29] J. Fanchi, Integrated reservoir asset management: principles and best practices. Gulf Professional Publishing, 2010.

[30] K. M. Pillai, "Governing equations for unsaturated flow through woven fiber mats. part 1. isothermal flows," Composites Part A: Applied Science and Manufacturing, vol. 33, no. 7, pp. 1007–1019, 2002.

[31] H. Darcy, Les fontaines publiques de la ville de Dijon: exposition et application... Victor Dalmont, 1856.